

Article

Plasmonic Nanoholes in a Multichannel Microarray Format for Parallel Kinetic Assays and Differential Sensing

Hyungsoon Im, Antoine Lesuffleur, Nathan C. Lindquist, and Sang-Hyun Oh

Anal. Chem., **2009**, 81 (8), 2854-2859 • DOI: 10.1021/ac802276x • Publication Date (Web): 13 March 2009

Downloaded from <http://pubs.acs.org> on May 12, 2009

More About This Article

Additional resources and features associated with this article are available within the HTML version:

- Supporting Information
- Access to high resolution figures
- Links to articles and content related to this article
- Copyright permission to reproduce figures and/or text from this article

[View the Full Text HTML](#)



ACS Publications
High quality. High impact.

Plasmonic Nanoholes in a Multichannel Microarray Format for Parallel Kinetic Assays and Differential Sensing

Hyungsoon Im, Antoine Lesuffleur, Nathan C. Lindquist, and Sang-Hyun Oh*

Laboratory of Nanostructures and Biosensing, Department of Electrical and Computer Engineering, University of Minnesota, Twin Cities, 200 Union Street South East, Minneapolis, Minnesota 55455

We present nanohole arrays in a gold film integrated with a six-channel microfluidic chip for parallel measurements of molecular binding kinetics. Surface plasmon resonance effects in the nanohole arrays enable real-time, label-free measurements of molecular binding events in each channel, while adjacent negative reference channels can record measurement artifacts such as bulk solution index changes, temperature variations, or changing light absorption in the liquid. With the use of this platform, streptavidin–biotin specific binding kinetics are measured at various concentrations with negative controls. A high-density microarray of 252 biosensing pixels is also demonstrated with a packing density of 10^6 sensing elements/cm², which can potentially be coupled with a massively parallel array of microfluidic channels for protein microarray applications.

Surface plasmon resonance (SPR) techniques enable real-time, label-free measurements of biomolecular binding kinetics and affinity,^{1,2} and play an important role for drug discovery and proteomics research. In contrast to radioactive or fluorescent labeling methods, label-free SPR kinetic assays provide unique advantages: (1) ligand–analyte binding kinetics can be probed without the costly and time-consuming labeling process that may also interfere with molecular binding interactions; (2) key biophysical parameters (binding rates and affinity) can be measured directly, as opposed to the mere presence of binding events; and (3) a wide range of molecular interactions, especially low affinity interactions that require high protein concentrations for saturation, can be characterized with less reagent consumption than other equilibrium measurement techniques.

Surface plasmons (SPs) are electromagnetic surface waves propagating at the interface between a metallic film and a dielectric medium³ and coupled to the free electron plasma in the metal. One of the key features of SPs is the tight confinement of the electromagnetic energy in the form of an exponentially decaying evanescent field within 100–200 nm of the surface, making SPs more sensitive to local refractive index changes than bulk

measurement techniques. Because of the hybrid nature of SP waves (photons bound with electrons), they cannot be excited directly by light and require a special experimental setup to increase the momentum of the incident photons. The most common way to excite SPs for biosensing applications is using a prism in a total internal reflection mode, known as the Kretschmann configuration. Binding of analytes to ligands immobilized on the gold sensor surface changes the local refractive index, which in turn induces a shift in the SPR excitation angle or wavelength.^{1,2} While the Kretschmann setup has been used successfully in the commercial BIAcore instruments for relatively low-throughput experiments, the bulky coupling prism sharply tilts the detection plane from the sample plane. If the Kretschmann setup is coupled with an imaging sensor for high-throughput experiments, as in SPR microscopy,^{4–8} the image of the sample surface is projected on the sensor surface with a large tilt angle, leading to defocusing and optical aberrations, prohibiting the use of high numerical aperture (NA) imaging lenses, and limiting the available field-of-view.⁸

Recent advances in protein microarray technology show promise for high-throughput studies of thousands of protein–protein interactions at a high spatial density.^{9,10} While existing protein microarray technology has relied on fluorescently labeled query molecules, modifying these molecules often changes their binding interactions. Avoiding the use of labels is highly desired but rarely realized, so it is a logical step to combine label-free kinetic SPR sensing with protein microarrays. Furthermore, integrating SPR technology and a high-density protein microarray can dramatically accelerate the accumulation of kinetics information about protein–protein and protein–nucleic acid interactions. Toward the ambitious goal of proteome-scale label-free kinetic assays, a new class of SPR instrument is needed that combines (1) high imaging resolution to collect kinetics data from individual spots on high-density microarrays; (2) massively parallel multiplexing capability and a large field-of-view; and (3) a simple and robust optical design.

(4) Yeatman, E.; Ash, E. A. *Electron. Lett.* **1987**, *23*, 1091–1092.

(5) Rothenhäusler, B.; Knoll, W. *Nature* **1988**, *332*, 615–617.

(6) Smith, E. A.; Corn, R. M. *Appl. Spectrosc.* **2003**, *57*, 320A–332A.

(7) Shumaker-Parry, J. S.; Aebersold, R.; Campbell, C. T. *Anal. Chem.* **2004**, *76*, 2071–2082.

(8) Chinowsky, T. M.; Mactutus, T.; Fu, E.; Yager, P. *Proc. SPIE* **2004**, *5261*, 173–182.

(9) MacBeath, G.; Schreiber, S. L. *Science* **2000**, *289*, 1760–1763.

(10) Ramachandran, N.; Hainsworth, E.; Bhullar, B.; Eisenstein, S.; Rosen, B.; Lau, A.; Walter, J. C.; LaBaer, J. *Science* **2004**, *305*, 86–90.

* To whom correspondence should be addressed. E-mail: sang@umn.edu. Phone: 612-625-0125.

(1) Liedberg, B.; Nylander, C.; Lunström, I. *Sens. Actuators* **1983**, *4*, 299–304.

(2) Homola, J.; Yee, S. S.; Gauglitz, G. *Sens. Actuators, B* **1999**, *54*, 3–15.

(3) Ritchie, R. H. *Phys. Rev.* **1957**, *106*, 874–881.

The extraordinary optical transmission (EOT) effect in periodic nanohole arrays in a metallic film¹¹ provides unique opportunities for building such high-throughput SPR instruments using a simple microscope setup. When light is incident on a thin gold film perforated with arrays of periodic subwavelength holes, SP waves are launched via a grating coupling mechanism, “funneling” light through the holes, which is reradiated on the opposite side. The peak transmission wavelengths for normally incident light can be approximated by¹¹

$$\lambda_{\text{peak}} \approx \frac{a_0}{\sqrt{i^2 + j^2}} \sqrt{\frac{\epsilon_m \epsilon_d}{\epsilon_m + \epsilon_d}} \quad (1)$$

where a_0 is the periodicity of the nanohole array, i and j are the grating orders, and ϵ_m and ϵ_d are the dielectric constants of the metal and dielectric, respectively. Since SPs play a central role in the transmission,^{12–14} the position of λ_{peak} is sensitive to local refractive index changes on the surface, as with SPR biosensors using a prism coupler.^{15–27} While nanohole SPR sensors have a lower bulk refractive index sensitivity than the prism-based equivalent,^{15,18,21} they nevertheless provide overall advantages for a high-throughput imaging implementation by eliminating optical design constraints imposed by the prism. Especially important are that the signal can be measured with normally incident optical geometry, enabling high imaging resolution, easy optical alignment, and a large field-of-view, all of which are critical for high-density protein microarray applications. Following the proof-of-concept by Brolo et al.,¹⁵ several groups have demonstrated SPR biosensing based on the EOT effect.^{16–27} We have previously demonstrated real-time kinetic sensing with shape-enhanced sensitivity using nanohole arrays²¹ and multiplex SPR microarray sensing using a laser source and a CCD camera.²³

In this work, we integrate periodic nanoholes within a linear array of microfluidic channels to demonstrate multiplex SPR

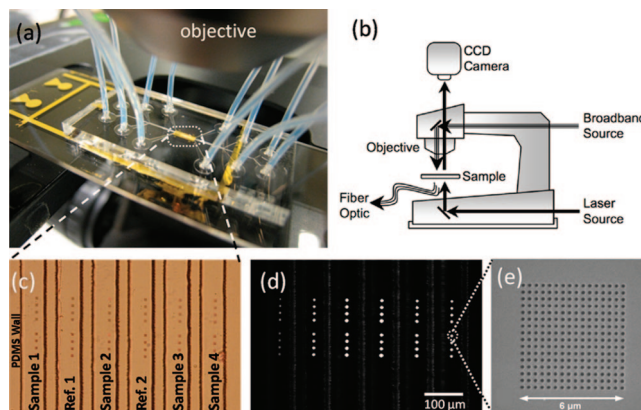


Figure 1. (a) Image of the microfluidic chip on a microscope stage with Teflon tubes connected to a syringe pump to control the flow of each solution. (b) Schematic of the measurement system, showing a broadband lamp for spectral measurements and bright-field image capture, and the laser source for real-time multiplex SPR imaging with the CCD camera. (c) A bright-field microscope image of six parallel microfluidic channels permitting the delivery of different solutions to different nanohole array sensors. (d) A transmission mode image using a 10× microscope objective. The periodicities of the arrays range from 390 to 420 nm and are illuminated from below with a 633 nm HeNe laser beam. (e) SEM image of one of the nanohole arrays. The array consists of 16 × 16 nanoholes, and each nanohole is 150 nm in diameter.

microarray imaging and differential sensing of streptavidin–biotin binding kinetics using a laser-based multiplex imaging platform we reported previously.²³ Here, each microfluidic channel in the chip contains a series of nanohole array sensing elements with tuned resonance wavelengths. Negative controls and analytes of different concentrations are injected into individual channels, enabling parallel, differential data acquisition as well as the subtraction of unwanted background signals arising from noise sources such as temperature change, bulk liquid index change, and mechanical vibrations. The experimental results are compared with computational modeling using three-dimensional (3-D) finite-difference time-domain (FDTD) simulations.

EXPERIMENTAL SECTION

Instrumentation and Real-Time Data Acquisition. Figure 1 shows the experimental setup for differential nanohole array based SPR imaging. Figure 1a shows a complete ready-to-use device, consisting of a patterned gold-coated glass slide with integrated microfluidics, set on a microscope stage where the optical detection is performed. Teflon tubing connected to the microfluidic channels allows addressing each nanohole array with various solutions, i.e., various concentrations of analytes with negative controls. Figure 1b is a schematic representing the optical detection system built around an upright bright field microscope. This setup can be used either for real-time spectral measurement using a broadband halogen lamp source and a fiber optic spectrometer or for real-time multiplex imaging experiments using a laser source and a CCD camera. In this paper, we present results obtained with the imaging configuration using a HeNe laser at 632.8 nm and a deep-cooled CCD camera (Photometrics Cool SNAP HQ²). The laser spot size was 800 μm. The HeNe laser illuminates the sample from below, through the glass substrate, exciting surface plasmons and EOT effects in the patterned

- (11) Ebbesen, T. W.; Lezec, H. J.; Ghaemi, H. F.; Thio, T.; Wolff, P. A. *Nature* **1998**, *391*, 667–669.
- (12) Barnes, W. L.; Murray, W. A.; Dintinger, J.; Devaux, E.; Ebbesen, T. W. *Phys. Rev. Lett.* **2004**, *92*, 107401/1–107401/4.
- (13) Gao, H. W.; Henzie, J.; Odom, T. W. *Nano Lett.* **2006**, *6*, 2104–2108.
- (14) Liu, H.; Lalanne, P. *Nature* **2008**, *452*, 728–731.
- (15) Brolo, A. G.; Gordon, R.; Leathem, B.; Kavanagh, K. L. *Langmuir* **2004**, *20*, 4813–4815.
- (16) Williams, S. M.; Rodriguez, K. R.; Teeters-Kennedy, S.; Stafford, A. D.; Bishop, S. R.; Lincoln, U. K.; Coe, J. V. *J. Phys. Chem. B* **2004**, *108*, 11833–11837.
- (17) Stark, P. R. H.; Halleck, A. E.; Larson, D. N. *Methods* **2005**, *37*, 37–47.
- (18) Tetz, K.; Pang, L.; Fainman, Y. *Opt. Lett.* **2006**, *31*, 1528–1530.
- (19) Stewart, M. E.; Mack, N. H.; Malyarchuk, V.; Soares, J. A. N. T.; Lee, T. W.; Gray, S. K.; Nuzzo, R. G.; Rogers, J. A. *Proc. Natl. Acad. Sci. U.S.A.* **2006**, *103*, 17143–17438.
- (20) De Leebeek, A.; Kumar, L. K. S.; de Lange, V.; Sinton, D.; Gordon, R.; Brolo, A. G. *Anal. Chem.* **2007**, *79*, 4094–4100.
- (21) Lesuffleur, A.; Im, H.; Lindquist, N. C.; Oh, S.-H. *Appl. Phys. Lett.* **2007**, *90*, 243110/1–243110/3.
- (22) Pang, L.; Hwang, G. M.; Slutsky, B.; Fainman, Y. *Appl. Phys. Lett.* **2007**, *91*, 123115/1–123115/3.
- (23) Lesuffleur, A.; Im, H.; Lindquist, N. C.; Lim, K.; Oh, S.-H. *Opt. Express* **2008**, *16*, 219–224.
- (24) Coe, J. V.; Heer, J. M.; Teeters-Kennedy, S.; Tian, H.; Rodriguez, K. R. *Annu. Rev. Phys. Chem.* **2008**, *59*, 179–202.
- (25) Gordon, R.; Sinton, D.; Kavanagh, K. L.; Brolo, A. G. *Acc. Chem. Res.* **2008**, *41*, 1049–1057.
- (26) Ji, J.; O’Connell, J. G.; Carter, D. J. D.; Larson, D. N. *Anal. Chem.* **2008**, *80*, 2491–2498.
- (27) Yang, J.-C.; Ji, J.; Hogle, J. M.; Larson, D. N. *Nano Lett.* **2008**, *8*, 2718–2724.

gold film. The transmitted laser light (as a bright spot from each nanohole array) is then collected using a 10 \times microscope objective (NA = 0.30) and imaged using the CCD camera. Figure 1c shows a bright-field microscope image of a six-channel device, where the PDMS (described below) walls and flow channels on the gold sensing surface are indicated. In each channel, eight nanohole arrays with different periodicities are used for real-time, label-free biosensing measurements. Multichannel devices are required to perform experiments with negative controls, or with various concentrations and protein interaction measurements, in a multiplexed manner. Figure 1d shows the same device in transmission mode, i.e., only illuminated from below by the HeNe laser beam. A custom-built MATLAB suite of analytical and signal processing code was used to control the CCD camera, capture image files at regular intervals of several seconds to several minutes, and process the image data to extract intensity profiles across the periodic nanohole microarray. For each image captured, rapid multiframe averaging was used to increase the signal-to-noise ratio. The response of a single sensor spot was quantified by integrating the transmitted intensity through each nanohole array. A syringe pump (Harvard apparatus PHD2000) was used to inject sample solutions at flow rates ranging from 2 μ L/h to 100 μ L/min.

Nanohole Array Fabrication. Standard glass microscope slides were first cleaned with acetone, methanol, isopropyl alcohol (IPA), and deionized water in ultrasonic baths for 15 min each. Optical lithography with Shipley 1813 positive photoresist was used to define the active gold region where the nanohole arrays were to be patterned. An e-beam evaporator (CHA, SEC600) was used to deposit a 5 nm chromium adhesion layer and a 200 nm thick gold film on the glass slides. Nanohole arrays were patterned with focused ion beam (FIB) milling using a 30 keV and 30 pA ion beam (FEI Dual Beam Quanta 200 3D). A typical sensing element, as shown in Figure 1e, consisted of a 16 \times 16 nanohole array with a footprint of 40 μ m². The nanohole diameter was 150 nm. The periodicities of the nanohole arrays ranged between 390 and 440 nm with 10 nm intervals.

Microfluidic Chip Fabrication and Integration. Soft lithography²⁸ with polydimethylsiloxane (PDMS, Sylgard) was used to fabricate a microfluidic flow cell for kinetic measurements of molecular bindings. The negative-tone master mold of the channel was patterned on a silicon wafer using SU-8 50 photoresist (ChemBio), defining 50 μ m deep and 50 μ m wide channels. A 10:1 ratio of PDMS and curing agent was degassed in vacuum and cast to be 3 mm thick over the SU-8 photoresist pattern. After curing the PDMS at 70 $^{\circ}$ C overnight, the PDMS flow cell was cut from the master, and inlet and outlet holes were punched for tubing connections. Prior to final assembly, the nanohole array substrate was cleaned thoroughly with acetone, IPA, and deionized water and dried in a stream of high-purity N₂. The nanohole array device was then cleaned under UV ozone. After the PDMS was cleaned with acetone, IPA, and deionized water, the surfaces of the PDMS channel and the sample slide were treated with a 50 W O₂ plasma for 10 s and covalently bonded to seal the flow channel. The PDMS flow cell was aligned with the nanohole arrays on the sample slide using a contact aligner (Karl Suss MJB3).

Functionalization of Nanohole Array Surface. Streptavidin and 11-amino-1-undecanethiol hydrochloride were purchased from Pierce and Sigma-Aldrich, respectively. The 11-amino-1-undecanethiol hydrochloride solution was prepared in double deionized water, and the concentration was adjusted to be 3 mM. Sulfo-NHS-LC-biotin (Pierce) solution was prepared in a 0.1 M sodium carbonate solution, with the final concentration adjusted to be 3 mM. Through the PDMS fluidic channels, the 11-amino-1-undecanethiol hydrochloride solution was injected at a 2 μ L/h flow rate over 24 h to form a self-assembled monolayer (SAM) of 11-amino-1-undecanethiol, followed by double deionized water washing. The nanohole array device with the SAM was then incubated with the sulfo-NHS-LC-biotin carbonate buffer solution for 12 h, followed by a PBS wash. The biotinylation solution was specially prepared for each experiment due to the quick hydrolysis of NHS esters. The gold surface was then treated with 0.2% bovine serum albumin (BSA) to reduce the nonspecific binding of streptavidin on the surface. After being rinsed with PBS, different concentrations of streptavidin/PBS solution, from 20 nM to 3 μ M, were injected through each microfluidic channel and the binding events of streptavidin and biotin from each nanohole array were measured in real-time.

RESULTS AND DISCUSSION

Figure 2a shows 3-D finite-difference time-domain (FDTD, Fullwave RSoft Design Group) simulations of several transmission spectra from two different nanohole arrays (with periodicities of 400 and 440 nm) as the refractive index of the surrounding medium is changed from that of water ($n = 1.333$) to that of ethanol ($n = 1.36$). As the refractive index increases, the transmission peak red-shifts, per eq 1, and the transmitted intensity of each nanohole array changes for a fixed wavelength. With dependence on the periodicity, the transmitted intensity can either decrease (400 nm periodicity) or increase (440 nm periodicity) at a fixed illumination wavelength ($\lambda = 633$ nm) as the refractive index increases from 1.333 to 1.36. This is due to the sign of the slope of the transmission peak at 633 nm: positive for a periodicity of 400 nm and negative for a periodicity of 440 nm. These FDTD results are consistent with the measured transmission spectra and intensity changes we reported previously.²³

Figure 2b shows the transmitted intensity change at 633 nm versus the refractive index for two different arrays. For periodicities of 400 and 440 nm, the transmitted intensity either linearly decreases or increases, respectively, as the refractive index increases from 1.33 to 1.36. The transmitted intensity change is directly related to the slope of the transmission spectrum at 633 nm and the amount of spectral shift due to the changing refractive index. For SPR imaging, the sensitivity of the nanohole arrays depends both on the spectral shift due to the refractive index change and on the slope of the transmission peak at the illumination wavelength.²³ Designing a good sensor, then, is a matter of choosing a periodicity where the illumination wavelength lies directly at the highest slope region of the transmission spectrum. Figure 2c shows the calculated and measured sensitivity (fractional intensity change versus refractive index change) for nanohole arrays with several periodicities. Of note is that for a periodicity of 420 nm, the transmission spectrum has a minimum around the 633 nm illumination wavelength, meaning that even

(28) Xia, Y. N.; Whitesides, G. M. *Angew. Chem., Int. Ed.* **1998**, *37*, 550–575.

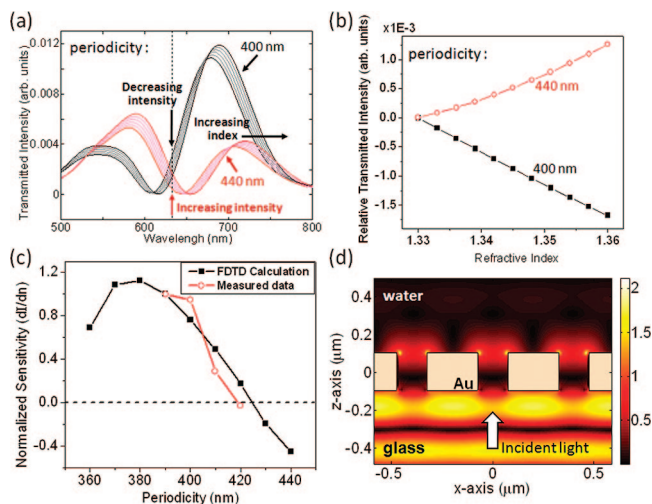


Figure 2. (a) FDTD calculations of the transmitted intensity through a nanohole array with 400 nm (black lines) and 440 nm (red lines) periodicities incubated in various media with refractive indices varying from 1.33 to 1.36. With dependence on the sign of the slope of the transmitted spectra at the illumination wavelength used (633 nm for a HeNe laser), the intensity either decreases (black lines) or increases (red lines) as the refractive index increases. (b) With the transmission sampled at 633 nm, the intensity is seen to decrease for a periodicity of 400 nm (black dots) and increase for a periodicity of 440 nm (red circles) as the refractive index increases. The intensities for both periodicities at $n = 1.33$ are shifted to zero for comparison. (c) Experimental and calculated normalized sensitivity (fractional change in transmitted intensity versus refractive index change) for various nanohole array periodicities. The sensitivity goes to nearly zero for a periodicity of 420 nm, since at that point, the illuminating wavelength (633 nm) lies at a transmission minimum, where the slope of the transmission spectrum is nearly zero. (d) Cross-sectional view of the calculated electric field intensity distribution for a periodic array of circular nanoholes. The incident light from below (glass substrate), via the EOT mechanism, is converted into surface plasmons which probe the local refractive index on the output (water) side of the gold film.

while the spectrum shifts, the transmitted intensity changes very little, giving poor sensitivity.

Figure 2d shows the calculated 3-D electric field intensity distribution at a transmission resonance for a periodicity of 400 nm. The illuminating field is seen from below (glass), and the exponentially decaying plasmonic field is seen on the top (water) side of the gold nanoholes. There, the presence of biomolecules can sharply modulate the plasmonic resonant conditions, shifting the resonant wavelength and modulating the transmitted intensity.

Figure 3a shows real-time experimental measurements of the transmitted intensity through several nanohole arrays when mixtures of water and ethanol at different concentrations are sequentially injected. First, deionized (DI) water ($n = 1.333$) is injected at a flow rate of 100 $\mu\text{L}/\text{min}$. Then, an increasing concentration of ethanol was used to vary the refractive index from 1.338 to 1.353. Finally, DI water was injected again to recover the initial transmitted intensity level. For the refractive index values from 1.333 to 1.353, the transmitted intensity linearly decreases with each increasing refractive index step for all periodicities except 420 nm, where the 633 nm HeNe illumination samples the nanohole array at a transmission minimum. These are in good agreement with the FDTD calculations presented in parts b and c of Figure 2.

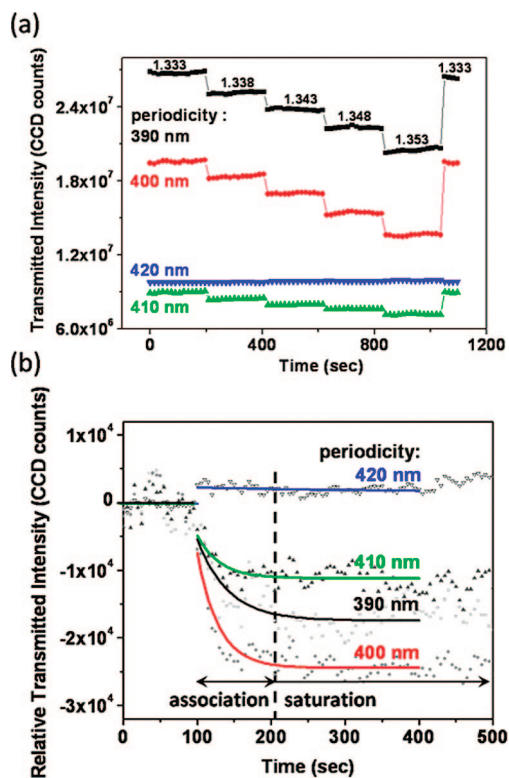


Figure 3. (a) Continuously measured transmission intensity, which depends on the bulk refractive index change due to various ethanol in water solutions and on the periodicities of the nanohole arrays, which range from 390 to 420 nm. (b) Real-time streptavidin–biotin binding kinetics measurement. The concentration of streptavidin is 100 nM. As more binding events occur, the intensity decreases for periodicities of 390, 400, and 410 nm, while it remains relatively flat for a periodicity of 420 nm.

Nanohole array sensing elements were arranged in a multi-channel microarray format to monitor the specific binding of streptavidin and biotin under different experimental conditions and with multiple negative controls. In SPR measurements of ligand–analyte binding, it is important to perform separate control experiments to rule out nonspecific binding of the analyte onto the gold surface or to correct for refractive index artifacts due to changes in the bulk solution index. This is especially important when a high concentration of analyte sample is injected, a common condition for measuring very weak interactions, where the bulk refractive index artifact or light absorption can be significant, causing a large shift in the measured SPR signal before any specific binding events occur. It should be noted that in the Kretschmann setup, which operates in a reflection mode, the source light does not traverse the liquid sample, whereas in a nanohole SPR sensor, light transmission is measured through a liquid flow cell. Therefore it is necessary to measure the light absorption in the sample solution. If these artifacts are not taken into account, the binding affinity cannot be precisely quantified. This differential sensing scheme can also eliminate background fluctuations such as temperature, source intensity, and vibration without having to use more sophisticated mechanisms, such as on-chip temperature control. In our multichannel platform, each microfluidic channel can be functionalized with a different type of molecule which can subsequently interact with different analytes, allowing concurrent measurements of positive/negative

controls and analytes of varying concentrations. Furthermore, each microfluidic channel includes a series of nanohole sensing elements, each with different resonance wavelength, enabling us to “scan” different sections of the EOT spectra.

The laser transmission through each nanohole array is modulated by the bulk refractive index change of an analyte solution and also by the binding of streptavidin molecules to the immobilized biotin molecules. Two types of negative control samples were used in our experiment. Since no specific binding can occur between the streptavidin and the SAM, a PDMS microchannel without immobilized biotin served as a negative control. Another microchannel was filled with a phosphate buffered saline (PBS) buffer as a negative control to monitor system fluctuations. Those negative controls were placed adjacent to the active sensing region, with 50 μm spacing as shown in Figure 1. The microfluidic channels were initially filled with the PBS solution. Then, the six-channel PDMS chip was used to deliver different concentrations of streptavidin in a PBS solution at a flow rate of 2 $\mu\text{L}/\text{h}$.

Figure 3b shows real-time measurements of biotin–streptavidin binding events with different nanohole array periodicities. The concentration of streptavidin is 100 nM, and the periodicities of the nanohole arrays ranged from 390 to 420 nm with 10 nm intervals. First, the streptavidin solution was injected at a high flow rate of 100 $\mu\text{L}/\text{min}$ for 150 s to establish the measurement baseline and to measure the bulk refractive index difference between the initial PBS buffer and the streptavidin solution before specific binding occurs on the surface. Then the flow rate was reduced to 2 $\mu\text{L}/\text{h}$, and the transmitted intensity decayed exponentially in time as more streptavidin bound to the biotin immobilized on the surface, before finally saturating. The variation of the transmitted intensity depended on the periodicity of the array, as discussed in Figure 3a. For a nanohole array with a 400 nm periodicity, the transmitted intensity drops due to biotin–streptavidin binding on the surface are bigger than other periodicities because the 633 nm laser wavelength is located at the transmission resonance region with the highest slope, while for a nanohole array with a 420 nm periodicity, the transmitted intensity remains fairly constant with the same molecular binding, because 633 nm corresponds to the minimum of transmission where the slope is close to zero. Therefore, to achieve the highest sensitivity, precise tuning of nanohole array periodicity is needed to position the laser wavelength at the region of the sharpest slope.

To investigate the detection limit of the sensor for biotin–streptavidin binding and to rule out nonspecific binding, different concentrations of streptavidin solution with corresponding negative controls, which do not have immobilized biotin in the channels, were injected into parallel channels. From six channels, only four channels were incubated with biotin for measuring binding kinetics with different concentrations of streptavidin of 20, 30, 50, and 100 nM. The other two reference channels were incubated with a biotin-free buffer solution for negative controls and injected with 50 and 100 nM streptavidin solutions.

Figure 4a shows binding kinetics measured for different concentrations of streptavidin (20, 30, 50, and 100 nM) from nanohole arrays with a 400 nm periodicity. The transmitted intensity decreases, at saturation, by 6.5%, 8.9%, and 18.8% for concentrations of 30, 50, and 100 nM, respectively. The red curves

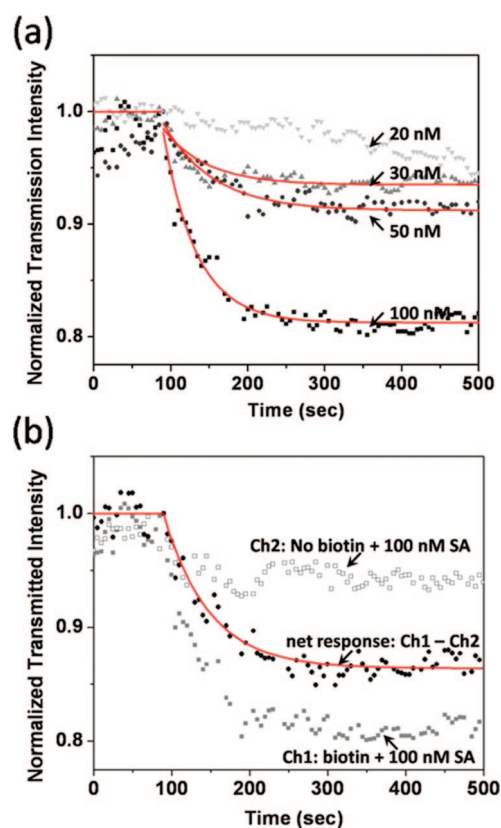


Figure 4. (a) Real-time streptavidin–biotin binding kinetics measured for different concentrations of streptavidin (20, 30, 50, and 100 nM) from the nanohole arrays. Down to 30 nM, the measured data fits the curve from a simple bimolecular binding model ($A + B \leftrightarrow AB$). (b) Real-time differential sensing of streptavidin and biotin binding kinetics is obtained by plotting the difference between measurements from two neighboring microfluidic channels separated by 100 μm . Biotin is immobilized in one channel only, while 100 nM streptavidin solutions are simultaneously injected into both channels at the same flow rate of 2 $\mu\text{L}/\text{h}$.

show a least-squares fit to the measured data for each concentration, following binding responses based on a simple biomolecular reaction model.²⁹ Calculations based on the data presented in Figure 4a gives the affinity constant to have a value of $4.12 \times 10^6 \text{ M}^{-1}$. This value is fairly close to a previously reported²⁹ value of $7.3 \times 10^6 \text{ M}^{-1}$. As the concentration of streptavidin goes below 20 nM, the transmitted intensity change is comparable to the noise level, making it difficult to accurately fit a curve.

Figure 4b shows differential sensing of streptavidin and biotin binding kinetics using two neighboring microfluidic channels. The net binding kinetics between streptavidin and biotin was obtained by subtracting the measurement in the reference channel, which does not have immobilized biotin, from the data obtained in the sample channel functionalized with biotin wherein a 100 nM streptavidin solution was injected at a flow rate of 2 $\mu\text{L}/\text{h}$, demonstrating the ability of the multichannel platform to account for experimental artifacts. The transmitted intensity change from the reference channel is 5–7%. This is due not only to nonspecific bindings of streptavidin onto the Au surface but also due to the bulk refractive index change. The multichannel platform is able to simultaneously measure binding kinetics with different con-

(29) Tang, Y.; Mernaugh, M.; Zeng, X. *Anal. Chem.* **2006**, *78*, 1841–1848.

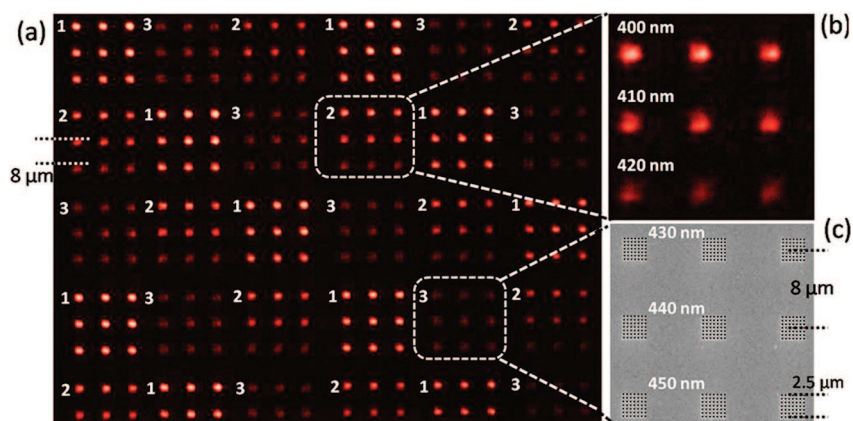


Figure 5. (a) Transmission image of a large microarray with 252 nanohole arrays, each one separated by 8 μm . The periodicity of each nanohole array is varied from 370 to 450 nm, giving different transmission intensities. The arrays are grouped as 3×3 subarrays, where each subarray has three different periodicities. (370–390 nm for group 1, 400–420 nm for group 2, and 430–450 nm for group 3) (b) Enlarged image of a 3×3 subarray. Each row has the same periodicity, which varies by 10 nm for the next row. (c) Scanning electron micrograph of one of the 3×3 subarrays. Each nanohole array consists of 7×7 nanoholes, each with a diameter of 150 nm.

centrations with corresponding negative controls, enabling differential sensing of binding kinetics while removing experimental artifacts.

Figure 5 shows a microarray of 252 sensing elements, wherein the periodicity of each nanohole array sensing element ranges from 370 to 450 nm. The center-to-center distance between each array is 8 μm , which gives the packing density of 1.45×10^6 arrays per cm^2 . Figure 5a shows the CCD image of the nanohole arrays in transmission, illuminated from below with a HeNe laser. The zoomed image of a 3×3 subarray is shown in Figure 5b. Each row, consisting of three sensing elements, has the same periodicity, which is varied by 10 nm for each row. Figure 5c is a scanning electron micrograph of one of the subarrays. Each sensing element is a single 7×7 nanohole array. The SP-enhanced light transmission is modulated as the periodicity of each 7×7 nanohole array is scaled. This demonstrates the possibility of packing the nanohole array sensing elements at a density that is not achievable with standard SPR biosensors. While the FIB fabrication method used for this work does not lend itself to large-area patterning, emerging technologies such as soft interference lithography,³⁰ nanoimprint lithography,³¹ or colloidal templating techniques³² are able to print nanometer-sized patterns over centimeter-sized areas. The combination of multiplex SPR sensing using a simple microscope setup with differential sensing for accurate quantification shows promise for using this platform for high-throughput studies of protein–protein interactions.

SUMMARY AND CONCLUSION

Plasmonic nanohole arrays were combined with a linear array of microfluidic channels for multiplex measurements of molecular

binding kinetics and differential SPR sensing. Specific biotin–streptavidin binding was characterized with varying concentrations and multiple negative controls. Simultaneous measurements of unique binding interactions in each of the six channels were demonstrated. The platform demonstrated here combines high packing density, stable laser-illumination, multiplex detection, and differential sensing capability, all of which are essential for nanohole SPR sensors to compete with existing SPR instruments for quantifying molecular binding kinetics with high throughput. It will also be possible to reduce the width of each microfluidic channel and the channel-to-channel gap to below $\sim 20 \mu\text{m}$, which will allow the potential integration of hundreds of parallel microfluidic channels with this platform. Finally, an array packing density of $\sim 10^6$ sensing spots per cm^2 has been achieved, showing the potential of scaling up the SPR multiplexing capacity of the nanohole array platform³³ toward the goal of massively parallel kinetic assays of protein–protein interactions on high-density protein microarrays.

ACKNOWLEDGMENT

S.-H.O. gratefully acknowledges support from a 3M Non-Tenured Faculty Award and Minnesota Partnership for Biotechnology and Medical Genomics. H. Im was supported by 3M Science and Technology Fellowship and N.C.L. by NIH Biotechnology Training Grant No. T32-GM008347. Device fabrication was performed at the University of Minnesota NanoFabrication Center, which receives support from the NSF National Nanotechnology Infrastructure Network (NNIN).

Received for review October 28, 2008. Accepted February 18, 2009.

AC802276X

- (30) Henzie, J.; Lee, M. H.; Odom, T. W. *Nat. Nanotechnol.* **2007**, *2*, 549–554.
- (31) Chou, S. Y.; Krauss, P. R.; Renstrom, P. J. *Appl. Phys. Lett.* **1995**, *67*, 3114–3116.
- (32) Sun, C.-H.; Min, W.-L.; Jiang, P. *Chem. Commun.* **2008**, 3163–3165.
- (33) Lindquist, N. C.; Lesuffleur, A.; Im, H.; Oh, S.-H. *Lab Chip* **2009**, *9*, 382–387.